

Research papers

Digital rock analysis for accurate prediction of fractured media permeability



Hamed Lamei Ramandi*, Peyman Mostaghimi, Ryan T. Armstrong

School of Petroleum Engineering, The University of New South Wales, Sydney, NSW 2052, Australia

ARTICLE INFO

Article history:

Received 9 April 2016

Received in revised form 23 June 2016

Accepted 15 August 2016

Available online 20 August 2016

This manuscript was handled by P. Kitanidis, Editor-in-Chief, with the assistance of Niklas Linde, Associate Editor

Keywords:

Fractured media
Micro-CT imaging
Digital rocks
Fracture aperture
Permeability

ABSTRACT

Determining the permeability of fractured rocks depends significantly on fracture geometry and topology. To date, no practical approach has been proposed to produce realistic binary images of fractured rocks from micro-computed tomography (micro-CT) images for fluid flow simulation. In this paper, a novel method is developed for generating a binary image that contains the true characteristics of fractured rocks for accurate computation of permeability. The method employs high-resolution scanning electron microscope (SEM) data for calibration of micro-CT images. Micro-CT is used to obtain 3D images of a highly fractured rock sample with a resolution of 16.5 μm and SEM is applied to obtain images with nanometer resolution from polished surfaces of the sample. The SEM images are then registered to the micro-CT images to facilitate image segmentation and generate a calibration curve. The calibration curve correlates the grayscale values at the midpoint of each fracture to the true aperture size measured from SEM data. Thinned fractures of two subsets are extracted and used to obtain the gray-scale values at the midpoint of fractures. These are converted to the true aperture value using the calibration curve and subsequently grown by an adjustment algorithm to produce 3D calibrated binary images that are representative of the true fracture system. The connectivity and aperture size distribution of the subsets before and after calibration are quantified. The permeability of the subsets before and after calibration are computed using a direct numerical simulator and compared with experimental measurements. The computed permeabilities demonstrate that using non-calibrated images generates massive permeability errors whereas calibrated images produce accurate permeability results that nearly coincide with experimental measurements. The method can be applied to fractured rocks for better prediction of permeability and other petrophysical properties.

© 2016 Elsevier B.V. All rights reserved.

1. Introduction

Permeability is a fundamental parameter that governs fluid transport in geologic media. Its magnitude and spatial distribution plays an important role in analyzing underground fluid migration and has been studied by numerous researchers (Bisdorn et al., 2016; Gangi, 1978; Gerami et al., 2016; Illman, 2006; Jazayeri Noushabadi et al., 2011; Latham et al., 2013; Nick et al., 2011; Norouzi Apourvari and Arns, 2016; Ramandi et al., 2016b; Scheidegger, 1963; Wang and Park, 2002). The flow capacity of fractured media is almost entirely controlled by the number and aperture size of fractures and continuity in the direction of flow whereas the contribution of the intact rock materials (unfractured region) to the total flow capacity, if any, is often relatively

small (Clarkson and Marc Bustin, 1996; Moore, 2012; Puri et al., 1991; Somerton et al., 1975). One of the most complex fractured porous media is coal in which a set of orthogonal fractures governs the flow. More than 50% (by weight) of the coal matrix is composed of macerals (Suárez-Ruiz and Crelling, 2008) that are organic discrete plant constituents (Crelling, 1989; Suárez-Ruiz and Crelling, 2008). The natural fracture system in coal typically contains two sets of orthogonal fractures, known as face and butt cleats, which are also orthogonal to the bedding plane (Laubach and Tremain, 1991; Laubach et al., 1998; Ting, 1977).

A variety of destructive (Brown et al., 1986; Gentier et al., 1989; Pyrack-Nolte et al., 1987) and nondestructive (Detwiler et al., 1999; Huo et al., 2016; Keller, 1998; Ketcham et al., 2010; Kumar et al., 1997; Mazumder et al., 2006; Renshaw et al., 2000; Robert et al., 1993; Van Geet and Swennen, 2001; Vandersteen et al., 2003; Verhelst et al., 1995; Yao et al., 2009) methods have been used for measuring fracture aperture sizes in rocks. Using a nondestructive method for characterization of a fractured rock is more

* Corresponding author.

E-mail addresses: h.lameiramandi@unsw.edu.au (H.L. Ramandi), peyman@unsw.edu.au (P. Mostaghimi), ryan.armstrong@unsw.edu.au (R.T. Armstrong).

advantageous since obtaining a fractured sample in which a permeable fracture network is preserved can be challenging (Ortega et al., 2006). When such a sample is obtained, prior to sample breakage, numerous experiments are required to be performed for petrophysical characterization. In the proposed nondestructive methods, digital rock imaging using X-ray micro-computed tomography (micro-CT) holds the advantage that it can be used for flow simulation (Armstrong et al., 2014a, 2014b; Berg et al., 2014; Huo et al., 2016).

A common problem with digital images acquired with micro-CT deals with the balance between obtaining a large enough representative image of the sample and the image resolution that is required to resolve accurate pore and/or fracture structure (Jing et al., 2016; Ramandi et al., 2016a, 2016b). While scanning larger samples, the image resolution in the direction normal to a fracture, is often not enough, and is often represented by only a few voxels (Ketcham et al., 2010). Micrometer-sized fracture aperture sizes typically occur near the resolution limit of the micro-CT instrument. This makes fracture network visualization and aperture size measurement problematic. In an air-filled (dry) micro-CT image, low attenuation coefficients (gray-scale values) are observed where a fracture exists. This is due to the density deficit caused by the lower density of the air-filled fractures than adjacent coal matrix regions. However, due to (i) smearing of the X-ray attenuation and (ii) partial volume effects, attenuation coefficients are reduced in the vicinity of a fracture (Ketcham, 2005; Ketcham and Carlson, 2001; Weerakone and Wong, 2010). The partial volume effect causes gray-scale values to reduce in voxels adjacent to fractures. This is because the voxel volume can contain various different materials, in this case fracture and matrix, which results in a gray-scale value that characterizes some average of the properties (Ketcham and Carlson, 2001). Moreover, when material properties change spatially over small distances, smearing of the X-ray attenuation occurs due to the finite beam width and over-sampling associated with the micro-CT instrument (Johns et al., 1993; Ketcham, 2005). As a result of these two limitations, the gray-scale transition between neighboring objects with different densities spans several voxels rather than being “sharp” which in turn result in mislabeling of fractures during the segmentation process and consequently gross overestimation/underestimation of aperture widths and thus fractured rock permeability (Ketcham, 2005).

A few alternative techniques have been proposed for measuring fracture aperture sizes using micro-CT data. These methods use the local gradient in voxel values from raw and/or filtered images. These include peak height (PH) (Mazumder et al., 2006; Vandersteen et al., 2003; Verhelst et al., 1995), full-width-half-maximum (FWHM) (Peyton et al., 1992), and missing attenuation (MA) (Johns et al., 1993; Mazumder et al., 2006; Vandersteen et al., 2003). PH carries the advantage that it is independent of fracture direction (Vandersteen et al., 2003) and can estimate relatively small aperture sizes (Mazumder et al., 2006). These approaches can be used either by creating a calibration curve (Mazumder et al., 2006) or using a calibration-free method (Huo et al., 2016). In the previous studies, the relationship between the FWHM, MA or PH and fracture aperture sizes is determined using careful calibration with spacers of known thickness, which allows for the generation of a calibration curve (Johns et al., 1993; Ketcham et al., 2010; Mazumder et al., 2006; Vandersteen et al., 2003). One drawback of these approaches is that they require at least two sets of micro-CT images; one for imaging fractures of known dimensions and another for the sample of interest. However, using this type of calibration curve for measuring aperture sizes in the image of interest involves potential measurement errors. This is because the proposed calibration curves fail to account for the variation of the attenuation coefficient with imag-

ing conditions. This variation results in obtaining images in which a fixed constituent is represented with different attenuation coefficients and to compensate for this images must be rescaled, which results in uncertainties. This suggests that each generated calibration curve is unique and cannot be used for images that are obtained at different imaging conditions. In addition, these previous methods have not been examined by comparison against a higher resolution method, e.g. SEM data. Lastly, the previous methods only provide a means to measure fracture aperture size and do not provide a way to use this data for the reconstruction of a more accurate 3D image of the fractures such that flow simulations are possible.

Recently Ramandi et al. (2016a) introduced a 2D technique in which SEM images that are registered to micro-CT data are used to generate the calibration curve. In this way, the need for acquiring two sets of micro-CT images and its problematic consequences of rescaling are eliminated. Nevertheless, a 3D method that can be applied to the micro-CT image to capture true fracture aperture sizes and thus reconstruct a calibrated 3D fracture network is lacking in the literature.

Herein, we report a novel framework in which we acquire a 3D image of a fractured rock sample at the core-scale and implement a workflow to obtain the characteristic structure of the sample and thus reconstruct a representative binary image for flow simulation. We initially execute an effective segmentation strategy to capture the entire fracture network of the sample. Then thin the fractures to a single voxel at the midpoint of the fracture aperture. The thinned fracture is subsequently used to extract gray-scale values at the midpoint of each fracture in the original micro-CT image. The extracted values are converted to aperture sizes using an SEM generated calibration curve. At this point, voxel values along the thinned fracture correspond to true aperture sizes. Then an adjustment algorithm proceeds to open the calibrated-thinned fracture according to the aperture values to create a binary image, which includes the correct geometry and connectivity. Herein, we validate the workflow by comparing fracture aperture sizes from SEM data and the presented calibration technique and also simulated and experimentally measured permeabilities.

2. Methodology

2.1. Data collection

For micro-CT imaging, a high-resolution helical scanner is used. The instrument is a part of the micro-CT facility at the Australian National University (Sheppard et al., 2014). The scanner settings are provided in Table 1. The collected projections from the instrument are reconstructed to produce a 3D representation of the sample (tomograms). Each data point in the tomogram characterizes the effective X-ray attenuation coefficient, which is displayed in 16-bit gray-scale images.

Table 1
The scanning parameters of the instrument used in this study.

Scanning parameters	Specifications
Acquisition time	23 h
Energy of X-ray	120 kV (100 mA)
Scanning operation	Helical system
X-ray beam form	Cone beam
Total number of projections	10,106
Pitch	25.938 mm
The angular step	0.002493 Rad
The vertical step	0.010293 mm
Beam hardening filter	3 mm aluminum

The selected sample for imaging is a coal sample with a diameter of 25 mm and length of 37 mm. The geology of the region and sample specifications are discussed in Ramandi et al., 2016b. The sample is initially scanned in as-received condition, i.e. dry air-filled fractures (Fig. 1a). For highlighting fluid-accessible pores and fractures the sample is saturated with an X-ray attenuating fluid and re-imaged, i.e. wet image with fluid-filled fractures (Fig. 1b). The X-ray attenuating fluid is a mixture of 1.5 M Sodium Iodide (NaI) and 1.0 M Potassium Chloride (KCl). The saturation process involves intrusion by X-ray attenuating fluid under vacuum for 1 day, and isostatic pressurization in X-ray attenuating fluid at a high pressure of ~670 bars for 1 week. In this way, the majority of the fluid-accessible pores and fractures are saturated. Micro-CT images, wet and dry, have a resolution of 16.5 μm . A cubic subset of 5.62 mm³ (M_1) and a rectangular prismatic subset of 3.3 \times 3.3 \times 2 mm (M_2) are obtained for testing the proposed method. These subsets contain well-developed fracture networks with a range of fracture aperture sizes above and below the image resolution. After micro-CT imaging the sample is cut and polished for SEM imaging. Secondary Electron and Backscatter Electron SEM techniques are accomplished using a Hitachi S3400 at the Electron Microscope Unit of the Mark Wainwright Analytical Centre at the University of New South Wales.

The dry and wet images are then registered using the technique developed by Latham et al. (2008). The method performs a voxel-to-voxel registration of the dry and wet images. The technique brings the dry and wet images into geometric alignment and generates a pair of images with identical dimensions allowing for a voxel-to-voxel comparison. Since the minerals and attenuating fluid-saturated pores and fractures are represented with approximately similar gray-scale values in the wet image, after image registration, dry and wet images are subtracted to provide the difference image. The difference image locates the fractured regions (Fig. 1c) and quantifies effective porosity of individual voxels that are not readily recognizable with conventional imaging techniques (Ramandi et al., 2015). This allows for the visualization of a more representative fracture network than obtained with conventional imaging of the dry sample.

The 2D-to-3D registration technique developed by Latham et al. (2008) is used to register SEM images to micro-CT images (Fig. 2). The algorithm searches the entire block of the tomogram to find the exact slice that matches the SEM image. Then the algorithm performs the required translation, rotation, warping and scaling transformations to coincide each point in the SEM data to the corresponding slice from the 3D tomogram. This allows for a direct comparison of the higher-resolution information provided in the SEM data to that in the micro-CT data, which assists in selection

of appropriate threshold levels and generation of a calibration curve.

2.2. Image processing

Micro-CT images contain attenuation coefficients that are displayed in a gray-scale image. Image segmentation involves converting the gray-scale image into unique well-defined regions (phases) that are homogeneous with respect to some characteristic (Sheppard et al., 2004). A bimodal intensity histogram for the sample that represents voids and intact matrix as individual peaks is ideal for image segmentation. However, there are often features at or below the instrument resolutions which blur sharp edges at phase boundaries (Ketcham, 2005; Sheppard et al., 2004). These blurred features spread out the intensity histogram and make visualization and segmentation difficult for complex multi-mineral and fractured samples. To remove noise and sharpen the images a non-linear anisotropic diffusion filter followed by an unsharp mask is applied (Sakellariou et al., 2007; Sheppard et al., 2004). These are shown to be highly effective at sharpening edges without excessively intensifying the noise (Sheppard et al., 2004). Converging active contours (CAC), which is developed based on a combination of the watershed method (Vincent and Soille, 1991) and active contour methods (Caselles et al., 1997), is used to yield satisfactory segmentation results. CAC uses intensity gradient and intensity information simultaneously (Schlüter et al., 2014; Sheppard et al., 2004) and has been successfully applied to cubic datasets of up to 2000³ voxels (Golab et al., 2013; Qajar et al., 2012; Ramandi et al., 2015, 2016b; Saadatfar et al., 2012a, 2012b; Sheppard et al., 2004; Sok et al., 2010). The algorithm proceeds by inputting two thresholds that are chosen through a detailed inspection of the gray-scale image histogram. The algorithm tags voxels with gray-values less than the lower threshold as void and voxels with gray-scale values greater than the upper threshold as solid. The values between the lower and upper thresholds are tagged as unallocated. The algorithm simultaneously expands the tagged regions towards each other, within the unallocated region, to place the boundary at the points where two contours join (Schlüter et al., 2014; Sheppard et al., 2004). The local gradient and distance of the local voxel value to the mean voxel value of its matching phase determine the speed at which the boundaries expand (Schlüter et al., 2014). We perform three successive CACs on the difference image to segment it into four phases: (1) resolved voids that include fractures and pores that are resolved using the micro-CT imaging technique (2) sub-resolution fractures and pores that exist below the micro-CT resolution limit, or exist at or above the micro-CT resolution limit but not resolved using the micro-CT

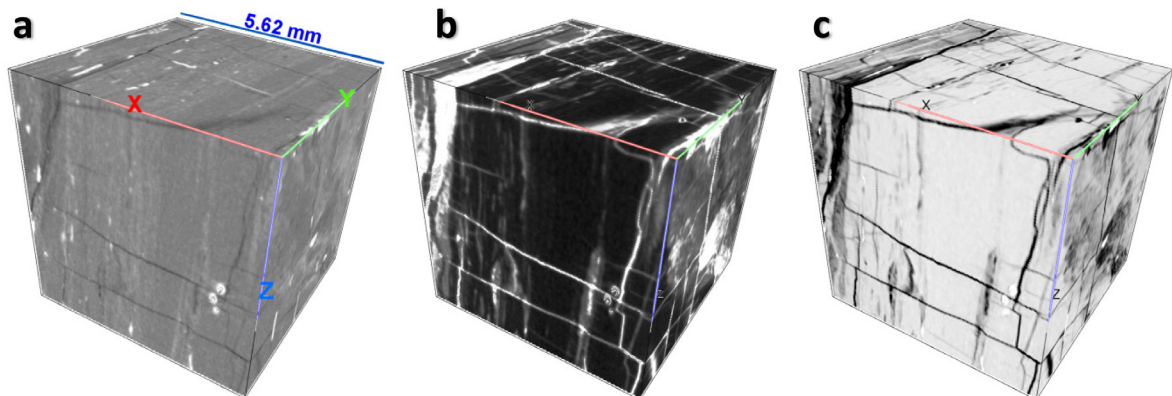


Fig. 1. (a) A registered 5.6 mm cube of dry micro-CT image (black = pores and fractures, gray = macerals and white = minerals), (b) the same cube after saturation with X-ray attenuating fluid (white = minerals and saturated pores and fractures, and black = macerals), (c) the difference image of the same cube (inverted difference image, black = pores and fractures, gray = macerals and white = minerals).

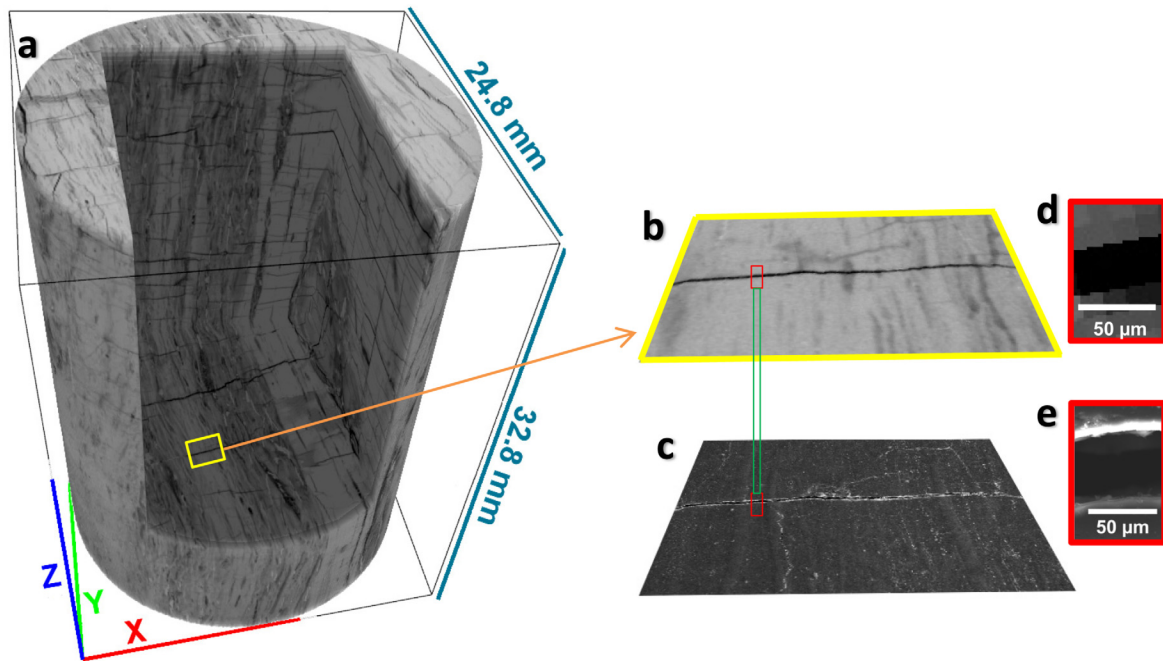


Fig. 2. Schematic of the 2D-to-3D image registration method. (a) A 3D image of a coal sample, (b) a 2D slice from the highlighted region in the 3D image of coal, (c) the registered SEM image of the same slice, (d) the enlarged portion of the region of interest of the micro-CT slice, and e: the same region from the registered SEM image.

imaging technique, (3) coal macerals that include organic regions of the coal that are not penetrated by X-ray attenuating fluid, and (4) mineral phases (inorganic) that included high density regions in the coal (Fig. 3b).

After applying the CAC segmentation two basic operations of mathematical morphology, dilation and erosion (Serra, 1986) are used to separate the sub-resolution pores from sub-resolution fractures. The erosion filter shrinks image features and eliminates features with a radius less than the kernel, while the dilation filter expand features in the image and close any gaps (Quackenbush, 2004). Erosion followed by dilation (opening) removes small or narrow elements without effecting large ones (Dong, 1997). Buie et al. (2007) applied morphological operations on a micro-CT image of bone to remove the small channels in bone. We erode the sub-resolution pores and fracture phase to remove the sub-resolution fractures. Then the eroded region is dilated to obtain its initial shape without the sub-resolution fractures. This is masked on the original image to obtain the intersection regions between the original image and eroded-dilated image. This separates the sub-resolution pores, i.e. intersection region, and sub-resolution fractures, i.e. the remaining regions (Fig. 3c). To avoid loss of details due to dilation and erosion operations, the kernel radius for this filter is made as small as possible while not removing the sub-resolution pores. After image segmentation, the 3D gray-scale and segmented images are visually inspected on a layer-by-layer basis to ensure that all of the phases are segmented correctly, which in turn results in obtaining the correct fracture connectivity (Fig. 4). Note that this step is only to identify sub-resolution fractures from sub-resolution pores. In subsequent steps, we re-calibrate the apertures sizes and thus any manipulation of fracture geometry by the opening algorithm is accounted for in the later steps.

2.3. Image calibration

To measure the aperture size at each fracture point, an equation that is derived from the calibration curve presented in Ramandi et al. (2016a) is used. For this method, fracture midpoint gray-

scale values obtained from micro-CT data are correlated to the true aperture sizes measured from high-resolution SEM data that are registered to the micro-CT data. For details on the generation of the calibration curve refer to our previous works (Mostaghimi et al., 2015a; Ramandi et al., 2016a). The equation is a linear correlation between aperture size in μm , A , and the gray-scale value, gs ,

$$A = 0.0717 \text{ } gs - 4544 \quad (1)$$

We use an upsampling method based on the Catmull-Rom interpolation (Catmull and Rom, 1974) to obtain a calibrated image with a voxel resolution greater than the original image. In this technique, the number of voxels are increased by a user-defined factor to generate an image with a less voxel size (Cantrell and Michaels, 2010; James, 2012; Leone et al., 2009). This allows for assigning aperture sizes smaller than the image resolution (Ramandi et al., 2016a). To extract the gray-values at the midpoint of each fracture, each non-calibrated segmented image is upsampled and thinned to a single voxel width. Because the existing 3D thinning algorithms (Lee et al., 1994; Lindquist et al., 1996; Lindquist and Venkatarangan, 1999; Pudney, 1998) are designed for tubular and porous structures, e.g. bones, vessels or rock pores, they do not provide a proper thinning of fractures with planner structures. This point will be discussed in the Results and discussion section. Alternatively, we use a stack of 2D skeletons in the direction of flow simulation to generate a thinned fracture. The constructed thinned fracture is then used to obtain coordinates of each fracture aperture midpoint. The coordinates are then used to acquire the gray-scale value at the midpoint of each fracture aperture from the upsampled dry micro-CT image. Subsequently, the calibration curve is applied to derive aperture sizes from the acquired gray-scale values. This generates a thinned fracture along which the weighting value of each voxel corresponds to the true aperture size. Lastly, the aperture adjustment algorithm marches along the thinned fracture and opens it according to the corresponding aperture values. This creates a new binary image in which the fracture network is obtained from the micro-CT images while aperture sizes are assigned based on the calibration curve obtained from high-resolution SEM data (Ramandi et al., 2016a).

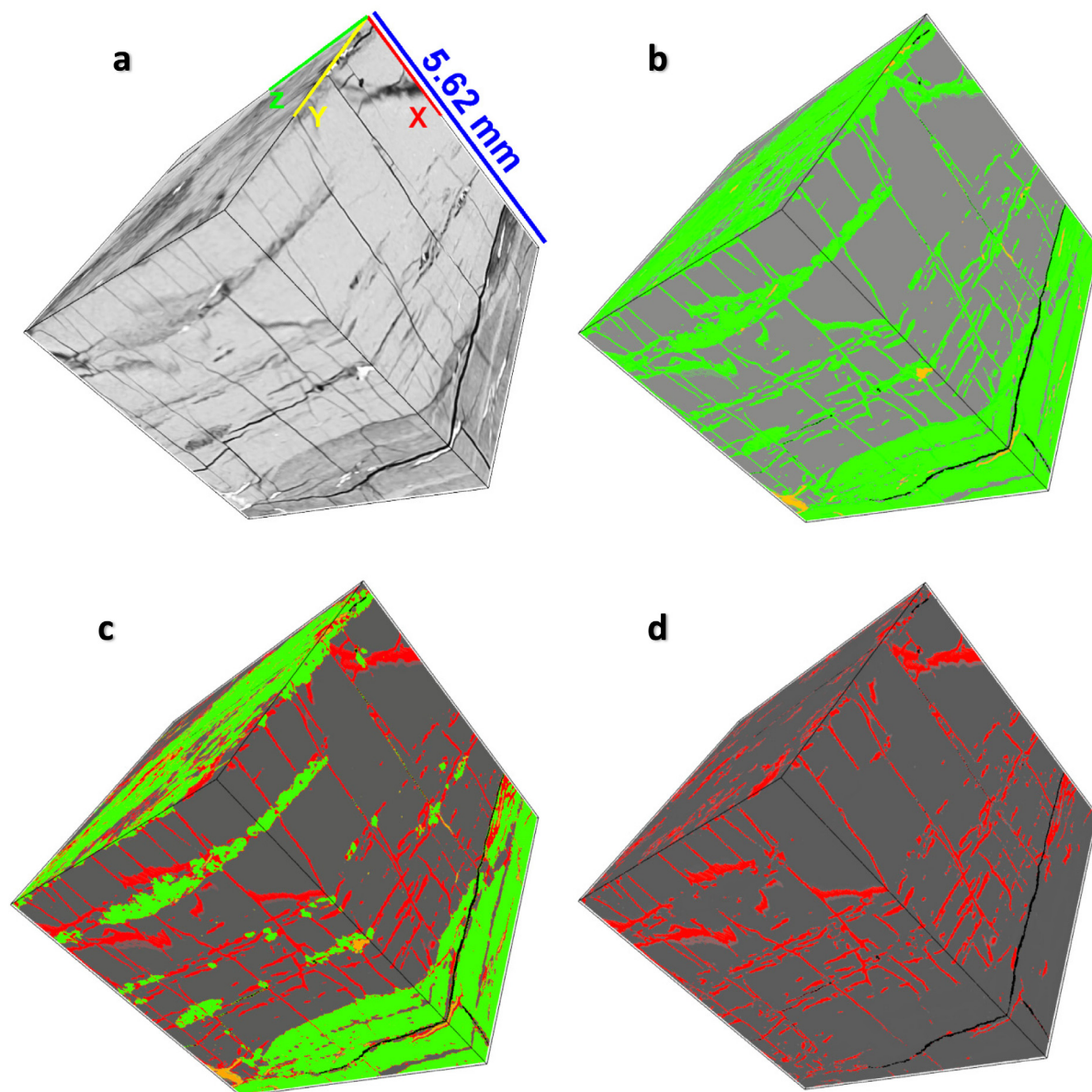


Fig. 3. 3D visualization of sample M₁. (a) The difference image (black = fractures and pores, gray = macerals and white = minerals), (b) the conventional segmented image (black = resolved fractures and pores, green = sub-resolution fractures and pores, gray = macerals, and orange = minerals), (c) segmented image using mathematical morphology (black = resolved fractures and pores, green = sub-resolution porous region, red = sub-resolution fractures, gray = macerals, and orange = minerals), (d) the fracture network of the sample (black = resolved fractures, red = sub-resolution fractures, gray = macerals). (For interpretation of the references to color in this figure legend, the reader is referred to the web version of this article.)

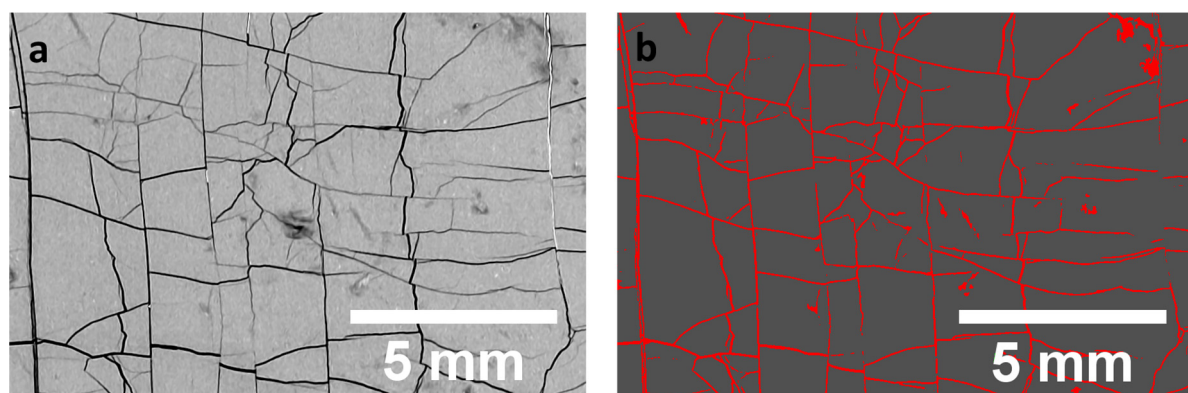


Fig. 4. An example of a layer-by-layer inspection of segmentation. (a) A slice of a difference image (black = fractures and pores, gray = macerals and white = minerals), (b) a slice of a segmented image showing the fracture network.

2.4. Connectivity and permeability measurement

Both the connectivity index and permeability measurements are used to quantify the resulting fracture networks and validate the presented method. The segmented image is used to identify the fracture network that percolates from inlet to outlet, using a voxel neighborhood connectivity requirement of 6 (Knackstedt et al., 2007). The percolating network is then used to measure the connectivity index. The connectivity index is a fundamental topologic measure that is defined as the maximum number of branches that can be broken within the network before splitting the network in half (Odgaard and Gundersen, 1993). The connectivity index is derived from Euler number, which is a topological invariant that defines the connectivity and/or topology of an object (Mecke, 1998; Odgaard and Gundersen, 1993).

$$\beta_1 = 1 - \Delta\chi \quad (2)$$

where β_1 is the connectivity index and $\Delta\chi$ is the Euler characteristic of the sample. Because connectivity depends on sample size, the connectivity density (CD) is used to show the degree of connectivity per unit volume (Odgaard and Gundersen, 1993). CD is a measure of the degree of connectivity of the percolating network normalized by total volume ($CD = \frac{\beta_1}{V}$).

After identifying the percolating cluster, flow can be simulated in the fractured medium using computational fluid dynamics methods to obtain pressure and velocity fields (Mostaghimi and Mahani, 2010; Mostaghimi et al., 2015b, 2014). Permeability prediction is obtained based on a finite volume solution of the Stokes equation

$$\mu \nabla^2 \bar{u} = \nabla P \quad (3)$$

where \bar{u} is the velocity vector, P is pressure, and μ is the fluid viscosity. No-flow boundary condition is applied on the solid surfaces and constant pressure boundary condition is considered for the inlet and outlet. The measured velocity field is used to calculate the total flux passing through the percolating cluster; the permeability is then calculated based on Darcy's law by inserting the values for pressure gradient and flux. More details on the flow simulator including the discretized forms of equations and convergence criteria can be found in Mostaghimi et al. (2013).

To determine the experimental permeability of the sample, an automated permeameter is used. The permeability measurement is based on the unsteady pressure fall-off method that is first developed by Jones (1972). The instrument comprises a tank, a quick-release Hassler-type core holder, pressure transducers, pressure manifolds, a temperature probe, control valves and a data acquisition system. The instrument conducts a quick transient pressure test to calculate the Klinkenberg corrected permeability (Jones, 1972). The instrument is able to measure sample permeabilities ranging from 0.001 to 10,000 mD. Prior to the measurement, the instrument is calibrated with a sample of known permeability to ensure that the highest accuracy is achieved. To run the experiment, while the downstream pressure valve is closed, helium gas is injected to the system to fill the tank, manifold and sample with an initial pressure of 200 psi. Once the pore pressure is stabilized, the downstream valve is opened and vented to atmospheric pressure, and helium flows through the core plug to initiate the transient pressure. The decay of pressure with time is recorded and used for the permeability calculation. The volumetric rate of helium flow at the inlet face of the core plug can be derived from the ideal gas law, since the compressibility factor is unity for helium at low pressure and room temperature.

3. Result and discussion

Fracture geometry and connectivity has a direct impact on the permeability of fractured rocks; therefore, it is critical to capture these parameters accurately for the measurement of flow properties from 3D images of fractured rocks. A particular problem associated with the partitioning of fractures from porous sub-resolution regions is that the gray-scale voxel values of both regions are similar. This makes segmentation of fractures challenging. In many cases fractures with aperture sizes near the resolution limit can connect larger dominant fractures and thus significantly influence the connectivity of the fracture system. In Figs. 3c and 4, we demonstrate the ability of mathematical morphological operations in separating the sub-resolution features and fractures. This provides a 3D binary image in which the entire fracture network that appears in the 3D gray-scale image is captured by the segmentation method. From visual inspection of the segmented and gray-scale images it can be seen that we capture both the dominant fractures and fractures with aperture sizes near the resolution limit (Fig. 4). This fracture network is then used as input data for the presented 3D calibration technique.

Along with capturing fracture connectivity, precise aperture measurement and assignment are the determining factors for measuring an accurate permeability. Fig. 5 shows an SEM image of a fracture in the sample that is registered to the corresponding micro-CT data. The non-calibrated segmented image is thinned to a voxel-wide skeleton and then gray-scale values along the thinned fracture are converted to true aperture sizes using the calibration curve. Comparison of aperture sizes measured from the SEM data (Fig. 5a) and the non-calibrated image (Fig. 5c) demonstrates that significant error occurs by mislabeling of voxels in the fractured region. However, comparison of the same region in the calibrated aperture data and the SEM data demonstrate that the error in measuring fracture aperture size is significantly reduced (Fig. 5e). Assuming laminar flow between parallel plates, for a point along a fracture with a width of w_f , the effective fracture permeability k_f can be calculated by $k_f = \frac{w_f^2}{12}$ (Snow, 1968; Witherspoon et al., 1980). Using this relationship for the fracture aperture sizes shown in Fig. 5 demonstrates that an error of about 89% and 20% in permeability could occur for the non-calibrated and calibrated segmentation methods, respectively. This suggests that more satisfactory results can be achieved when the proposed calibration technique is used.

The next step is to determine the best approach for extracting the midpoint fracture voxels from the segmented micro-CT image. Fig. 6a shows the segmented fractures while Fig. 6b and 6c demonstrate different methods to extract midpoint aperture voxels. Fig. 6b displays the results using a 3D medial axis extraction algorithm, as described by Lee et al. (1994), Lindquist et al. (1996), Lindquist and Venkatarangan (1999) and Pudney (1998). The results demonstrate that 3D generation of the medial axis for the fractured sample with planar structures fails to provide a thinned fracture network that preserves the correct structure and connectivity of the sample, which is visually evident in Fig. 6b. This is because the methods are designed to provide a medial axis for tubular or porous structures whereas fractures are long and planar. The medial axis in this context is not really what we require rather we want the fracture to be thinned to a single voxel at the midpoint of all regions along the fracture. An alternative method, which is used in this study, is to restrict the thinned fracture construction to a 2D plane and repeat this for the entire image, i.e. restrict the thinning algorithm to a stack of 2D planes. Fig. 6c demonstrates that this method provides a preserved thinned fracture network.

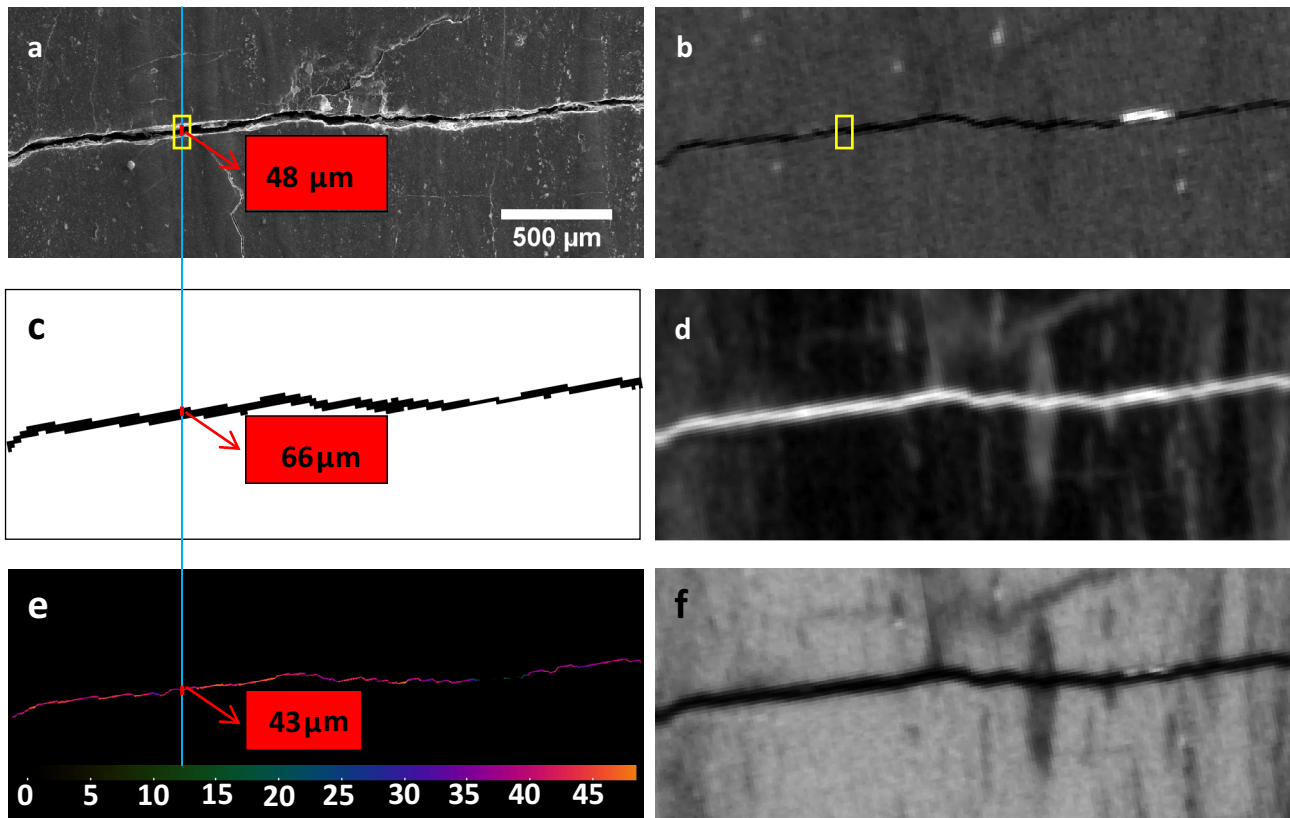


Fig. 5. (a) The registered SEM image (2.34 $\mu\text{m}/\text{pixel}$), (b) the registered dry micro-CT image (16.5 μm voxels, black = pores and fractures, gray = macerals and white = minerals), (c) segmented fracture from the same slice using non-calibrated segmentation method (16.5 μm voxels), (d) the registered wet micro-CT image (16.5 μm voxels, white = minerals and saturated pores and fractures, and black = macerals), (e) the weighted thinned fracture of the same slice, (f) the difference image of the same slice (16.5 μm voxels, inverted difference image, black = pores and fractures, gray = macerals and white = minerals).

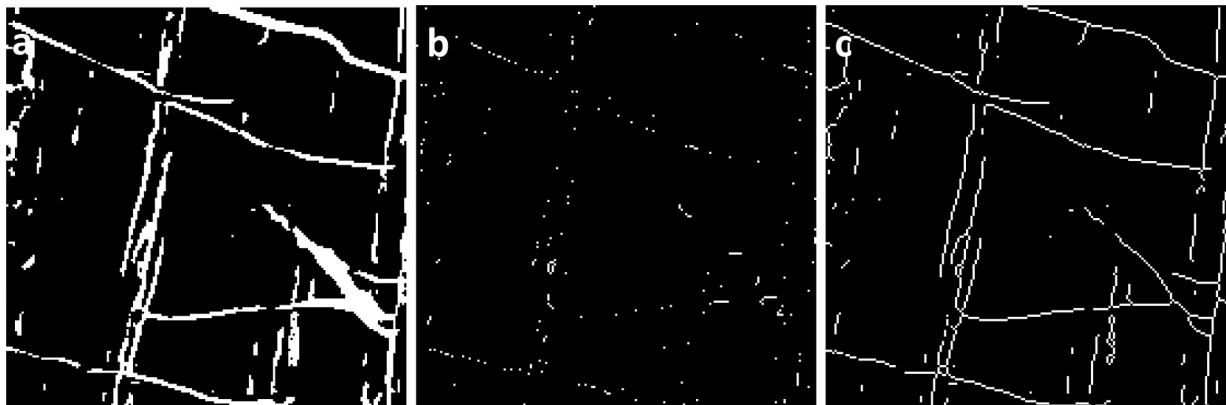


Fig. 6. The thinned fracture construction. (a) The entire fracture network, (b) constructed thinned fracture using 3D thinning algorithm, (c) constructed thinned fracture using stacks of skeleton in the direction of flow simulation.

Fig. 7 displays the fracture aperture size distribution for the percolating network of sample M_2 before and after applying the calibration curve. This demonstrates that a significant amount of data is disregarded when non-calibrated images are used. The calibration technique includes: (1) all of the fracture apertures with sizes smaller than the data resolution, and (2) fractures with aperture sizes larger than the resolution that are added to the connected flow network through new connections made by addition of the smaller fractures.

To demonstrate the importance of image calibration for accurate flow simulation, the permeability of M_1 and M_2 are initially

calculated for two different conditions: (1) assuming entire resolved and sub-resolution fractures are fully permeable, (2) assuming only resolved fractures are permeable. The results are shown in Table 2, a large difference between the two estimates is observed; however, none of the results are near the experimental permeability of ~ 110 mD. Using only resolved fractures underestimates the permeability and including sub-resolution and resolved fractures with no calibration overestimates the permeability. This indicates the significant error imposed by mislabeling sub-resolution fractures, i.e. condition (1) or ignoring sub-resolution fractures, i.e. condition (2).

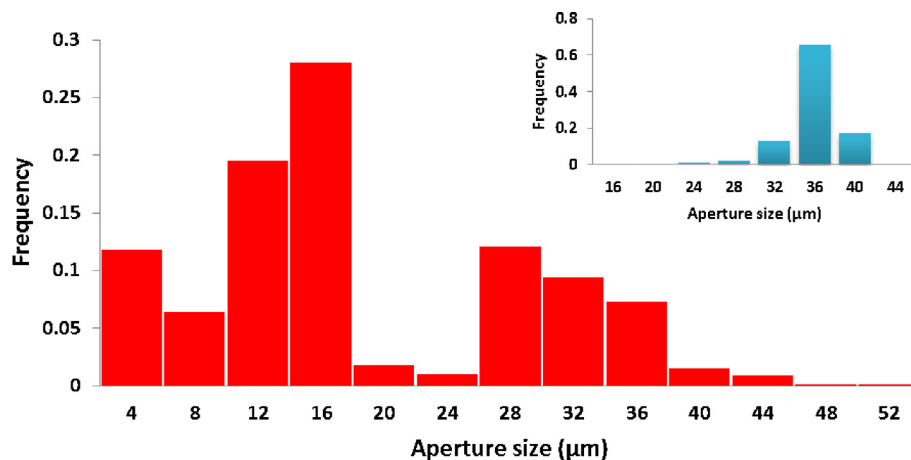


Fig. 7. Fracture aperture distribution of the percolating network in sample M₂ after calibration, and before calibration (the upper right graph).

Table 2

The permeability and connectivity results for sample M₁ and M₂ before and after calibration. Condition 1 assumes that entire resolved and sub-resolution fractures are fully permeable, i.e. mislabeling sub-resolution fractures. Condition 2 assumes that only resolved fractures are permeable, i.e. ignoring sub-resolution fractures.

Sample	Permeability mD			Connectivity density (mm ⁻¹)	
	Condition 1	Condition 2	Calibrated	Before	After
M ₁	3259	8.80E-03	90	1.54	816.09
M ₂	2627	5.85E-03	80	11.24	349.08

To calibrate the images, the subsets are upsampled by a factor of 4× to create images with a voxel size of ~4.1 μm. Then the segmented images are “thinned” and the corresponding aperture sizes are calculated using the equation derived from the calibration curve. Then the adjustment algorithm proceeds to open the weighted midpoint voxel aperture values to provide a 3D calibrated binary image for fluid flow simulation. Fig. 8 shows the connected fractures for sample M₂ before and after calibration. Since coal permeability largely originates from the fracture network and matrix permeability is orders of magnitudes lower than fracture permeability (Moore, 2012) the sub-resolution matrix

porosity is disregarded in the flow simulation. However, sub-resolution fractures that are added with the calibration technique are considered. Furthermore, if a connected pore system that is resolved by micro-CT is present in the rock mass it will contribute to the permeability simulation. The permeability results for the calibrated images are shown in Table 2. The results of the calibrated images are near the experimental permeability result with 18% and 27% error for M₁ and M₂, respectively. These in comparison with the errors caused by using a non-calibrated segmentation approach, which grossly differ from experimental permeability indicate the significant improvement that is achieved

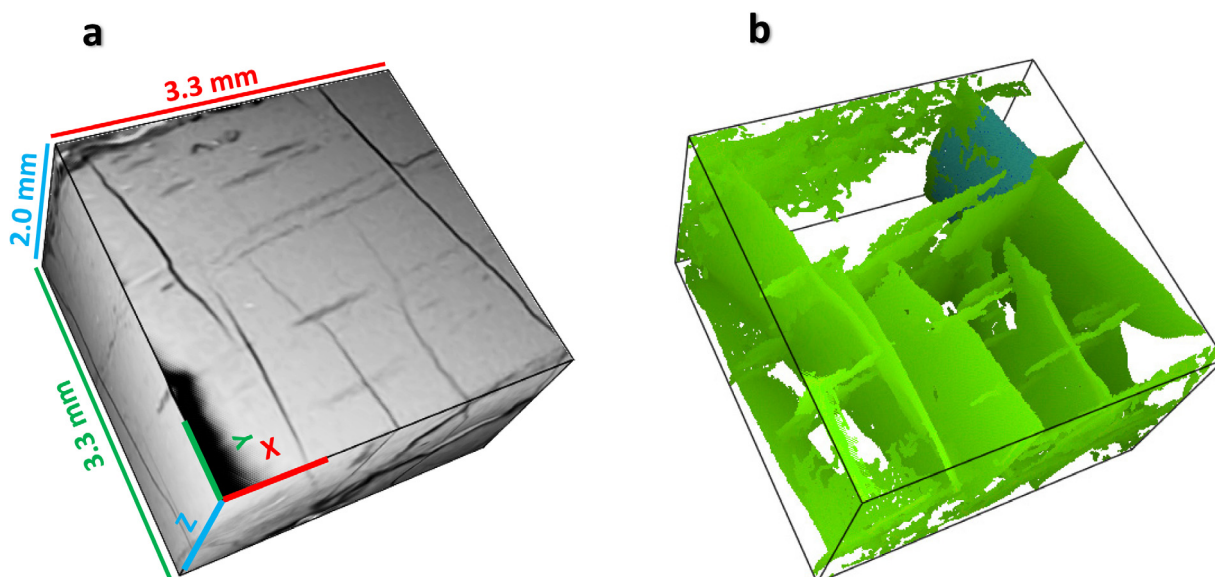


Fig. 8. 3D visualization of sample M₂. (a) The difference image of sample M₂ (black = pores and fractures, gray = macerals and white = minerals), (b) the connected fracture network of sample M₂ before and after calibration (blue region is the only percolating region in the non-calibrated image while the entire network (blue and green) is present in the connected network of calibrated image). (For interpretation of the references to color in this figure legend, the reader is referred to the web version of this article.)

through employing the calibration method. This occurs because the calibrated images include the resolved and sub-resolution fractures with correct aperture sizes.

Small errors observed in the calibrated images might be due to permeameter error, imaging noise, image resolution limitation, error in extracting thinned fractures, inaccuracies in the calibration curve, and/or disregarding the effect of nanometer-sized pores that cannot be resolved with micro-CT image. Preserving the original connectivity of the samples is critical for precise permeability calculation. However, there is now way of knowing *a priori* what is the true connectivity of the fracture systems. This requires image segmentation and thus the inherent errors involved. Hence, to ensure that the original connectivity of sample is preserved a layer-by-layer visual comparison between the 3D gray-scale and binary images is performed. To quantify the significance of including the entire network, connectivity density of sample M_1 and M_2 are measured before and after calibration. The results presented in Table 2 show a clear increase in the connectivity of samples after applying the calibration technique that in turn has a direct influence on permeability. Overall, the calibration technique allows for capturing connectivity and geometry of the fracture network that provides reasonable permeability calculations when direct numerical simulations are applied.

4. Conclusion and remarks

A novel framework was developed to assign accurate aperture sizes to the fracture structure extracted from micro-CT images. This resulted in calibrated 3D binary images in which flow simulation can be performed for computation of rock permeability. We used micro-CT to obtain pore-scale 3D digital images of a fractured rock sample in the air-filled and contrasting agent saturated conditions. Subtraction of these images reveals features near the resolution limit of the micro-CT instrument. Subsequent segmentation of the resolved and sub-resolution fracture network using CAC and mathematical morphological techniques provides an image in which the fracture network that appears in the 3D gray-scale image is well represented by the segmented image. Two subsets are obtained from the sample for petrophysical analyses. The subsets are upsampled by $4\times$ to enable assignment of aperture sizes less than the original data resolution. The gray-scale value at each fracture midpoint is extracted using a thinning algorithm applied to the segmented images. Then the gray-scale values are converted to aperture sizes using a calibration curve. Afterwards, the adjustment algorithm proceeds to grow the thinned fracture according to the calculated aperture sizes. This provides images in which apertures sizes are precisely assigned and original connectivities are preserved. The permeability of the images after and before calibration are computed and compared with experimental permeability. Also the connectivity and aperture size distribution of the images before and after calibration are measured. The calibrated images result in permeability values near the experimental result. The connectivity, aperture size measurements, and layer-by-layer comparison of images indicate that the presented calibration method preserves the true fracture geometry and connectivity and thus provides an accurate fracture network for flow simulations. Overall, the calibration technique allows for capturing connectivity and geometry of the fracture network that provides precise calculations of fractured rock permeability through direct numerical simulations.

References

- Armstrong, R.T., Georgiadis, A., Ott, H., Klemin, D., Berg, S., 2014a. Critical capillary number: desaturation studied with fast X-ray computed microtomography. *Geophys. Res. Lett.* 41, 55–60.
- Armstrong, R.T., Ott, H., Georgiadis, A., Rücker, M., Schwing, A., Berg, S., 2014b. Subsecond pore-scale displacement processes and relaxation dynamics in multiphase flow. *Water Resour. Res.* 50, 9162–9176.
- Berg, S., Armstrong, R., Ott, H., Georgiadis, A., Klapp, S., Schwing, A., Neiteler, R., Brussee, N., Makurat, A., Leu, L., 2014. Multiphase flow in porous rock imaged under dynamic flow conditions with fast X-ray computed microtomography. *Petrophysics* 55, 304–312.
- Bisdom, K., Bertotti, G., Nick, H.M., 2016. The impact of in-situ stress and outcrop-based fracture geometry on hydraulic aperture and upscaled permeability in fractured reservoirs. *Tectonophysics*. <http://dx.doi.org/10.1016/j.tecto.2016.04.006>.
- Brown, S.R., Kranz, R.L., Bonner, B.P., 1986. Correlation between the surfaces of natural rock joints. *Geophys. Res. Lett.* 13, 1430–1433. <http://dx.doi.org/10.1029/GL013i013p01430>.
- Buie, H.R., Campbell, G.M., Klinck, R.J., MacNeil, J.A., Boyd, S.K., 2007. Automatic segmentation of cortical and trabecular compartments based on a dual threshold technique for in vivo micro-CT bone analysis. *Bone* 41, 505–515.
- Cantrell, B., Michaels, W., 2010. *Digital Drawing for Landscape Architecture: Contemporary Techniques and Tools for Digital Representation in Site Design*. John Wiley & Sons.
- Caselles, V., Kimmel, R., Sapiro, G., 1997. Geodesic active contours. *Int. J. Comput. Vision* 22, 61–79.
- Catmull, E., Rom, R., 1974. A class of local interpolating splines. *Comput. Aided Geom. Des.* 74, 317–326.
- Clarkson, C.R., Marc Bustin, R., 1996. Variation in micropore capacity and size distribution with composition in bituminous coal of the Western Canadian Sedimentary Basin: implications for coalbed methane potential. *Fuel* 75, 1483–1498. [http://dx.doi.org/10.1016/0016-2361\(96\)00142-1](http://dx.doi.org/10.1016/0016-2361(96)00142-1).
- Crelling, J.C., 1989. Separation and characterization of coal macerals: accomplishments and future possibilities. *Am. Chem. Soc., Div. Fuel Chem.* 34 (1), 249–255.
- Detwiler, R.L., Pringle, S.E., Glass, R.J., 1999. Measurement of fracture aperture fields using transmitted light: an evaluation of measurement errors and their influence on simulations of flow and transport through a single fracture. *Water Resour. Res.* 35, 2605–2617. <http://dx.doi.org/10.1029/1999WR900164>.
- Dong, P., 1997. Implementation of mathematical morphological operations for spatial data processing. *Comput. Geosci.* 23, 103–107.
- Gangi, A.F., 1978. Variation of whole and fractured porous rock permeability with confining pressure. *Int. J. Rock Mech. Min. Sci. Geomech. Abstr.* 15 (5), 249–257.
- Gentier, S., Billiaux, D., Vliet, L., 1989. Laboratory testing of the voids of a fracture. *Rock Mech. Rock Eng.* 22, 149–157. <http://dx.doi.org/10.1007/BF01583959>.
- Gerami, A., Mostaghimi, P., Armstrong, R.T., Zamani, A., Warkiani, M.E., 2016. A microfluidic framework for studying relative permeability in coal. *Int. J. Coal Geol.* 159, 183–193. <http://dx.doi.org/10.1016/j.coal.2016.04.002>.
- Golab, A., Ward, C.R., Permana, A., Lennox, P., Botha, P., 2013. High-resolution three-dimensional imaging of coal using microfocus X-ray computed tomography, with special reference to modes of mineral occurrence. *Int. J. Coal Geol.* 113, 97–108. <http://dx.doi.org/10.1016/j.coal.2012.04.011>.
- Huo, D., Pini, R., Benson, S.M., 2016. A calibration-free approach for measuring fracture aperture distributions using X-ray computed tomography. *Geosphere* GES01175, 01171.
- Illman, W.A., 2006. Strong field evidence of directional permeability scale effect in fractured rock. *J. Hydrol.* 319, 227–236. <http://dx.doi.org/10.1016/j.jhydrol.2005.06.032>.
- James, J., 2012. *Digital Intermediates for Film and Video*. Focal Press, UK.
- Jazayeri Noushabadi, M.R., Jourde, H., Massonnat, G., 2011. Influence of the observation scale on permeability estimation at local and regional scales through well tests in a fractured and karstic aquifer (Lez aquifer, Southern France). *J. Hydrol.* 403, 321–336. <http://dx.doi.org/10.1016/j.jhydrol.2011.04.013>.
- Jing, Y., Armstrong, R.T., Ramandi, H.L., Mostaghimi, P., 2016. Coal cleat reconstruction using micro-computed tomography imaging. *Fuel* 181, 286–299. <http://dx.doi.org/10.1016/j.fuel.2016.04.127>.
- Johns, R.A., Steude, J.S., Castanier, L.M., Roberts, P.V., 1993. Nondestructive measurements of fracture aperture in crystalline rock cores using X ray computed tomography. *J. Geophys. Res.: Solid Earth* 98, 1889–1900. <http://dx.doi.org/10.1029/92JB02298>.
- Jones, S.C., 1972. A rapid accurate unsteady-state Klinkenberg permeameter. *Soc. Petrol. Eng. J.* 12, 383–397.
- Keller, A., 1998. High resolution, non-destructive measurement and characterization of fracture apertures. *Int. J. Rock Mech. Min. Sci.* 35, 1037–1050.
- Ketcham, R.A., 2005. Computational methods for quantitative analysis of three-dimensional features in geological specimens. *Geosphere* 1, 32–41.
- Ketcham, R.A., Carlson, W.D., 2001. Acquisition, optimization and interpretation of X-ray computed tomographic imagery: applications to the geosciences. *Comput. Geosci.* 27, 381–400. [http://dx.doi.org/10.1016/S0098-3004\(00\)00116-3](http://dx.doi.org/10.1016/S0098-3004(00)00116-3).
- Ketcham, R.A., Slottke, D.T., Sharp, J.M., 2010. Three-dimensional measurement of fractures in heterogeneous materials using high-resolution X-ray computed tomography. *Geosphere* 6, 499–514.
- Knackstedt, M.A., Arns, C.H., Sok, R.M., Sheppard, A.P., 2007. 3D pore scale characterisation of carbonate core: relating pore types and interconnectivity to petrophysical and multiphase flow properties. In: *International Petroleum Technology Conference, International Petroleum Technology Conference*.

- Kumar, A.T., Majors, P.D., Rossen, W., 1997. Measurement of aperture and multiphase flow in fractures using NMR imaging. *SPE Formation Eval.* 12, 101–108.
- Latham, J.-P., Xiang, J., Belayneh, M., Nick, H.M., Tsang, C.-F., Blunt, M.J., 2013. Modelling stress-dependent permeability in fractured rock including effects of propagating and bending fractures. *Int. J. Rock Mech. Min. Sci.* 57, 100–112. <http://dx.doi.org/10.1016/j.ijrmms.2012.08.002>.
- Latham, S., Varslot, T., Sheppard, A., 2008. Image registration: enhancing and calibrating X-ray micro-CT imaging. In: *Proc. of the Soc. Core Analysts*, Abu Dhabi, UAE.
- Laubach, S., Tremain, C., 1991. Regional coal fracture patterns and coalbed methane development. In: *The 32nd US Symposium on Rock Mechanics (USRMS)*, Norman, Oklahoma.
- Laubach, S.E., Marrett, R.A., Olson, I.E., Scott, A.R., 1998. Characteristics and origins of coal cleat: a review. *Int. J. Coal Geol.* 35, 175–207.
- Lee, T.C., Kashyap, R.L., Chu, C.N., 1994. Building skeleton models via 3-D medial surface axis thinning algorithms. *CVGIP: Graph. Models Image Process.* 56, 462–478. <http://dx.doi.org/10.1006/cgip.1994.1042>.
- Leone, P., Chow, W.-C., Gill, A., 2009. Chroma upsampling method and apparatus therefor. Google Patents.
- Lindquist, W.B., Lee, S.M., Coker, D.A., Jones, K.W., Spanne, P., 1996. Medial axis analysis of void structure in three-dimensional tomographic images of porous media. *J. Geophys. Res.: Solid Earth* 101, 8297–8310 (1978–2012).
- Lindquist, W.B., Venkatarangan, A., 1999. Investigating 3D geometry of porous media from high resolution images. *Phys. Chem. Earth Part A* 24, 593–599. [http://dx.doi.org/10.1016/S1464-1895\(99\)00085-X](http://dx.doi.org/10.1016/S1464-1895(99)00085-X).
- Mazumder, S., Wolf, K.H.A.A., Elewaut, K., Ephraim, R., 2006. Application of X-ray computed tomography for analyzing cleat spacing and cleat aperture in coal samples. *Int. J. Coal Geol.* 68, 205–222. <http://dx.doi.org/10.1016/j.coal.2006.02.005>.
- Mecke, K.R., 1998. Integral geometry in statistical physics. *Int. J. Mod. Phys. B* 12, 861–899.
- Moore, T.A., 2012. Coalbed methane: a review. *Int. J. Coal Geol.* 101, 36–81. <http://dx.doi.org/10.1016/j.coal.2012.05.011>.
- Mostaghimi, P., Armstrong, R.T., Gerami, A., Ebrahimi Warkaini, M., Ramandi, H., Lamei, Pinczewski, V., 2015a. Micro-CT imaging and microfluidics for understanding flow in coal seam reservoirs. In: *International Symposium of the Society of Core Analysts*, Newfoundland, Canada.
- Mostaghimi, P., Blunt, M.J., Bijeljic, B., 2013. Computations of absolute permeability on micro-CT images. *Math. Geosci.* 45, 103–125.
- Mostaghimi, P., Mahani, H., 2010. A quantitative and qualitative comparison of coarse-grid-generation techniques for modeling fluid displacement in heterogeneous porous media. *SPE Reservoir Eval. Eng.* 13, 24–36.
- Mostaghimi, P., Percival, J.R., Pavlidis, D., Ferrier, R.J., Gomes, J.L., Gorman, G.J., Jackson, M.D., Neethling, S.J., Pain, C.C., 2015b. Anisotropic mesh adaptivity and control volume finite element methods for numerical simulation of multiphase flow in porous media. *Math. Geosci.* 47, 417–440.
- Mostaghimi, P., Tollit, B.S., Neethling, S.J., Gorman, G.J., Pain, C.C., 2014. A control volume finite element method for adaptive mesh simulation of flow in heap leaching. *J. Eng. Math.* 87, 111–121.
- Nick, H., Paluszny, A., Blunt, M., Matthai, S., 2011. Role of geomechanically grown fractures on dispersive transport in heterogeneous geological formations. *Phys. Rev. E* 84, 056301.
- Norouzi Apourvari, S., Arns, C.H., 2016. Image-based relative permeability upscaling from the pore scale. *Adv. Water Resour.* <http://dx.doi.org/10.1016/j.advwatres.2015.11.005>.
- Odgaard, A., Gundersen, H., 1993. Quantification of connectivity in cancellous bone, with special emphasis on 3-D reconstructions. *Bone* 14, 173–182.
- Ortega, O.J., Marrett, R.A., Laubach, S.E., 2006. A scale-independent approach to fracture intensity and average spacing measurement. *AAPG Bull.* 90, 193–208.
- Peyton, R.L., Haeffner, B.A., Anderson, S.H., Gantzer, C.J., 1992. Applying X-ray CT to measure macropore diameters in undisturbed soil cores. *Geoderma* 53, 329–340. [http://dx.doi.org/10.1016/0016-7061\(92\)90062-C](http://dx.doi.org/10.1016/0016-7061(92)90062-C).
- Pudney, C., 1998. Distance-ordered homotopic thinning: a skeletonization algorithm for 3D digital images. *Comput. Vis. Image Underst.* 72, 404–413. <http://dx.doi.org/10.1006/cviu.1998.0680>.
- Puri, R., Evanoff, J., Brugler, M., 1991. Measurement of coal cleat porosity and relative permeability characteristics. In: *SPE Gas Technology Symposium*. Society of Petroleum Engineers, Houston, Texas.
- Pyrack-Nolte, L.J., Myer, L.R., Cook, N.G.W., Witherspoon, P.A., 1987. Hydraulic and mechanical properties of natural fractures in low-permeability rock. In: *Proc. 6th Int. Cong. Rock Mech.*, pp. 225–231.
- Qajar, J., Francois, N., Arns, C.H., 2012. Micro-tomographic characterization of dissolution-induced local porosity changes including fines migration in carbonate rock. *SPE J.* 18, 545–562. <http://dx.doi.org/10.2118/153216-PA>.
- Quackenbush, L.J., 2004. A review of techniques for extracting linear features from imagery. *Photogramm. Eng. Remote Sens.* 70, 1383–1392.
- Ramandi, H.L., Armstrong, R.T., Mostaghimi, P., 2016a. Micro-CT image calibration to improve fracture aperture measurement. *Case Stud. Nondestruct. Test. Eval.* <http://dx.doi.org/10.1016/j.csndt.2016.03.001>.
- Ramandi, H.L., Armstrong, R.T., Mostaghimi, P., Saadatfar, M., Pinczewski, W.V., 2015. X-ray micro-computed tomography imaging for coal characterization. In: *SPE Asia Pacific Unconventional Resources Conference and Exhibition*. Society of Petroleum Engineers. <http://dx.doi.org/10.2118/177017-MS>.
- Ramandi, H.L., Mostaghimi, P., Armstrong, R.T., Saadatfar, M., Pinczewski, W.V., 2016b. Porosity and permeability characterization of coal: a micro-computed tomography study. *Int. J. Coal Geol.* 154–155, 57–68. <http://dx.doi.org/10.1016/j.coal.2015.10.001>.
- Renshaw, C.E., Dadakis, J.S., Brown, S.R., 2000. Measuring fracture apertures: a comparison of methods. *Geophys. Res. Lett.* 27, 289–292. <http://dx.doi.org/10.1029/1999GL008384>.
- Robert, A.J., John, S.S., Louis, M.C., Paul, V.R., 1993. Nondestructive measurements of fracture aperture in crystalline rock cores using X ray computed tomography. *J. Geophys. Res.: Solid Earth* 98, 1889–1900. <http://dx.doi.org/10.1029/92JB02298> (1978–2012).
- Saadatfar, M., Francois, N., Arad, A., Madadi, M., Cruikshank, R., Alizadeh, M., Sheppard, A., Kingston, A., Limay, A., Senden, T., Knackstedt, M., 2012a. 3D mapping of deformation in an unconsolidated sand: a micro mechanical study. *SEG Tech. Program Expanded Abstr.* 2012. <http://dx.doi.org/10.1190/segam2012-1263.1>.
- Saadatfar, M., Mukherjee, M., Madadi, M., Schröder-Turk, G.E., Garcia-Moreno, F., Schaller, F.M., Hutzler, S., Sheppard, A.P., Banhart, J., Ramamurty, U., 2012b. Structure and deformation correlation of closed-cell aluminium foam subject to uniaxial compression. *Acta Mater.* 60, 3604–3615. <http://dx.doi.org/10.1016/j.actamat.2012.02.029>.
- Sakellariou, A., Arns, C.H., Sheppard, A.P., Sok, R.M., Averdunk, H., Limaye, A., Jones, A.C., Senden, T.J., Knackstedt, M.A., 2007. Developing a virtual materials laboratory. *Mater. Today* 10, 44–51. [http://dx.doi.org/10.1016/S1369-7021\(07\)70307-3](http://dx.doi.org/10.1016/S1369-7021(07)70307-3).
- Scheidegger, A.E., 1963. *The Physics of Flow through Porous Media*. University of Toronto.
- Schlüter, S., Sheppard, A., Brown, K., Wildenschild, D., 2014. Image processing of multiphase images obtained via X-ray microtomography: a review. *Water Resour. Res.* 50, 3615–3639. <http://dx.doi.org/10.1002/2014WR015256>.
- Serra, J., 1986. Introduction to mathematical morphology. *Comput. Vis. Graph. Image Process.* 35, 283–305.
- Sheppard, A., Latham, S., Middleton, J., Kingston, A., Myers, G., Varslot, T., Fogden, A., Sawkins, T., Cruikshank, R., Saadatfar, M., Francois, N., Arns, C., Senden, T., 2014. Techniques in helical scanning, dynamic imaging and image segmentation for improved quantitative analysis with X-ray micro-CT. *Nucl. Instrum. Methods Phys. Res., Sect. B* 324, 49–56. <http://dx.doi.org/10.1016/j.nimb.2013.08.072>.
- Sheppard, A.P., Sok, R.M., Averdunk, H., 2004. Techniques for image enhancement and segmentation of tomographic images of porous materials. *Physica A* 339, 145–151. <http://dx.doi.org/10.1016/j.physa.2004.03.057>.
- Snow, D.T., 1968. Rock fracture spacings, openings, and porosities. *J. Soil Mech. Found. Div.*
- Sok, R.M., Varslot, T., Ghous, A., Latham, S., Sheppard, A.P., Knackstedt, M.A., 2010. Pore scale characterization of carbonates at multiple scales: integration of micro-CT, BSEM, FIBSEM. *Petrophysics* 51, 379.
- Somerton, W.H., Söylemezoglu, I.M., Dudley, R.C., 1975. Effect of stress on permeability of coal. *Int. J. Rock Mech. Min. Sci. Geomech. Abstr.* 12, 129–145. [http://dx.doi.org/10.1016/0148-9062\(75\)91244-9](http://dx.doi.org/10.1016/0148-9062(75)91244-9).
- Suárez-Ruiz, I., Crelling, J.C., 2008. *Applied Coal Petrology: The Role of Petrology in Coal Utilization*. Academic Press.
- Ting, F.T.C., 1977. Origin and spacing of cleats in coal beds. *J. Press. Vess. Technol. Trans. ASME Ser. J.* 99, 624–626.
- Van Geet, M., Swennen, R., 2001. Quantitative 3D-fracture analysis by means of microfocus X-ray computer tomography (μ CT): an example from coal. *Geophys. Res. Lett.* 28, 3333–3336.
- Vandersteen, K., Busselen, B., Van Den Abele, K., Carmeliet, J., 2003. Quantitative characterization of fracture apertures using microfocus computed tomography. *Geol. Soc. 215*, 61–68. London, Special Publications.
- Verhelst, F., Vervoot, A., Bosscher, P.D., Marchal, G., 1995. X-ray computerized tomography: determination of heterogeneities in rock samples. In: *8th ISRM Congress*.
- Vincent, L., Soille, P., 1991. Watersheds in digital spaces – an efficient algorithm based on immersion simulations. *IEEE Trans. Pattern Anal.* 13, 583–598.
- Wang, J.A., Park, H.D., 2002. Fluid permeability of sedimentary rocks in a complete stress-strain process. *Eng. Geol.* 63, 291–300. [http://dx.doi.org/10.1016/S0013-7952\(01\)00088-6](http://dx.doi.org/10.1016/S0013-7952(01)00088-6).
- Weerakone, W.M.S.B., Wong, R.C.K., 2010. Characterization of variable aperture rock fractures using X-ray computer tomography. *Adv. X-ray Tomography Geomater.*, 229–235.
- Witherspoon, P.A., Wang, J.S., Iwai, K., Gale, J.E., 1980. Validity of cubic law for fluid flow in a deformable rock fracture. *Water Resour. Res.* 16, 1016–1024.
- Yao, Y., Liu, D., Che, Y., Tang, D., Tang, S., Huang, W., 2009. Non-destructive characterization of coal samples from China using microfocus X-ray computed tomography. *Int. J. Coal Geol.* 80, 113–123. <http://dx.doi.org/10.1016/j.coal.2009.08.001>.